Generic Multi-Frequency Modelling of Converter-Connected Renewable Energy Generators Considering Frequency and Sequence Couplings

Nouri, Behnam; Kocewiak, Lukasz Hubert; Shah, Shahil; Koralewicz, Przemyslaw; Gevorgian, Vahan; Sørensen, Poul

Published in:
IEEE Transactions on Energy Conversion

Link to article, DOI:
10.1109/TEC.2021.3101041

Publication date:
2022

Document Version
Peer reviewed version

Generic Multi-Frequency modelling of Converter-Connected Renewable Energy Generators Considering Frequency and Sequence Couplings

Behnam Nouri, *Student Member, IEEE,* Łukasz Kocewiak, *Senior Member, IEEE,* Shahil Shah, *Senior Member, IEEE,* Przemyslaw Koralewicz, *Member, IEEE,* Vahan Gevorgian, *Senior Member, IEEE,* and Poul Sørensen, *Fellow, IEEE,*

***Abstract*—Frequency and sequence couplings can compromise the trustworthiness of multi-frequency models for converter-based systems. There have been effective attempts to address the couplings mainly by linearized averaged models. Only a few studies have been conducted on practical optimization of such models with enormous matrices and experimental results. This paper provides a generic theory for coupling patterns and proposes a multi-frequency modelling method to detect and address only the main couplings in the sequence domain for converter-connected renewable energy generators. The proposed generic model is based on empirical tests using small-signal perturbations and adopting Fourier transform on the switching converter response. The proposed theory and modelling methodology are verified using a 7MVA grid emulator for voltage perturbation tests on a 2MVA photo-voltaic converter. Accordingly, the couplings can exist in more generic forms, including multiples of perturbation and fundamental frequencies. To the best of our knowledge, the patterns with the multiples of the perturbation frequency have been overlooked in the literature. Furthermore, the mirror frequency concept is valid for all coupling patterns and is included in the proposed model. Besides, the proposed patterns and the environment noise levels have been practical criteria for selecting the main couplings.**

***Index Terms*—Generic multi-frequency modelling, Frequency and sequence couplings, Perturbation test, Impedance modelling.**

NOMENCLATURE

REG	Renewable Energy Generators
WT	Wind Turbine
PV	Photo-Voltaic
LTP	Linear Time-Periodic
MMC	Modular Multi-level Converter
SISO	Single-Input Single-Output
MIMO	Multiple-Input Multiple-Output
MFC	Mirror Frequency Coupling
POC	Point Of Connection
PLL	Phase-Locked-Loop
SCR	Short Circuit Ratio
DFT	Discrete Fourier Transform

B. Nouri (beno@dtu.dk) and P. Sørensen are with the Department of DTU Wind Energy, Technical University of Denmark, 4000 Roskilde, Denmark.

Ł. Kocewiak is with the Ørsted, Nesa Allé 1, 2820 Gentofte, Denmark.

S. Shah, P. Koralewicz and V. Gevorgian are with National Renewable Energy Laboratory (NREL), CO, Golden, USA.

This work has received funding from the European Union's Horizon 2020 research and innovation program under grant agreement No. 691714.

I. Introduction

MULTI-FREQUENCY (harmonic) interaction is an increasing challenge in converter-dominated power systems, especially in renewable energy generation units. To date, several resonance issues and harmonic-related incidents have been reported from converter-based Renewable Energy Generators (REG), such as Wind Turbines (WT) and Photo-Voltaic (PV) converters, and HVDC systems [1]-[6]. Control dynamics and couplings in converters have been identified as the primary root causes of harmonic instability [6]-[9].

Small-signal linearization methods have been utilized to develop averaged models and explain the dynamics of power converters [7]-[11]. In [8]-[9], [11], a comparison of different analytical models is provided explicitly. Based on the harmonic linearization method, impedance-based modelling and analysis are introduced and developed for grid-connected converters in sequence-domain [11]-[16]. Besides, inspired by the harmonic linearization technique, the voltage or current perturbation tests have been used for multi-frequency model validations [13], [16]-[22].

Most of the multi-frequency models can be categorized in different reference frames, including synchronous frame (or dq-frame) and stationary frame ($\alpha\beta$-frame or sequence-domain) [19]. The dq-frame models are useful for control design and stability analysis but lack the analysis of unbalanced systems [8]-[9], [14], [19]. A variety of stationary-frame models are developed to enhance the models by including the effects of Phase-Locked-Loop (PLL) systems [13]-[14] [16], DC-link dynamics [16], [23], phase-dependent features [24], system asymmetries [25]-[26] and couplings [14], [23]-[33]. There has been special attention to the frequency and sequence couplings [14], [23]-[33], especially for Modular Multi-level Converters (MMC) [23], [25]-[33].

A typical example of a converter-connected REG is illustrated in Fig. 1. The averaged model of such converter-connected system is developed by describing the dynamics of the filter reactor current (i_f) as follows [9]-[16]:

$$L_f \frac{d}{dt}\begin{bmatrix} i_{fa} \\ i_{fb} \\ i_{fc} \end{bmatrix} = v_{dc}\begin{bmatrix} d_a \\ d_b \\ d_c \end{bmatrix} - \begin{bmatrix} v_{sa} \\ v_{sb} \\ v_{sc} \end{bmatrix} \tag{1}$$

where d_{abc} are the duty cycles for the switching converter derived from modulation of control reference voltage ($v_{abc(ref)}$)

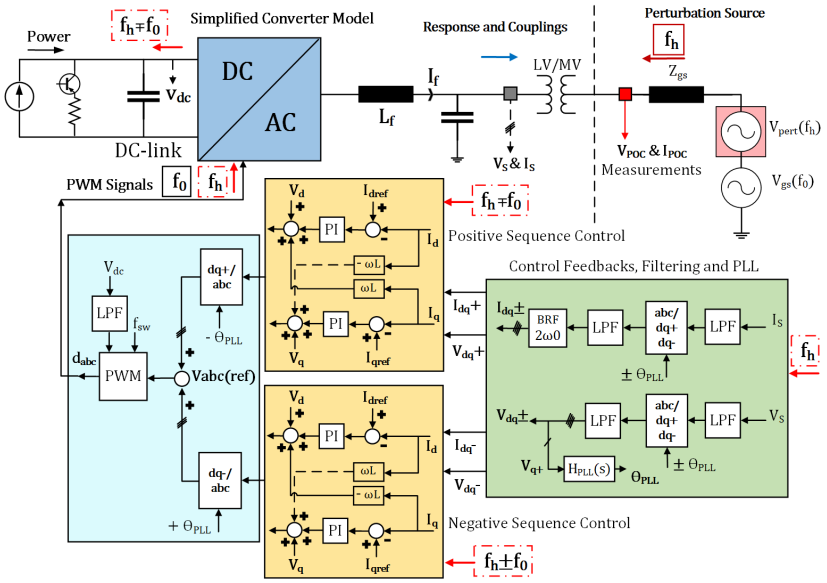

Fig. 1: Example illustration of a voltage perturbation interaction with a converter-connected REG with $dq^{\pm}$-frame control.

with carrier signal [9]-[16]. In the analytical models, the non-linear multiplication of v_{dc} and d_{abc} (representing $v_{abc(ref)}$) in (1) is simplified by linear terms within a small-signal range [9]-[16]; while it is the main root cause of couplings in switching converters.

Effects of the frequency and sequence couplings had been overlooked in the early stages of sequence-domain models [13]. In [14], [23], it is demonstrated that even small amplitudes of couplings could be important in converter stability. Consequently, the analytical models effectively improved by including the Mirror Frequency Coupling (MFC) in a matrix form [14]-[16], [19]. Given a small-signal perturbation at "f_i", the MFC is interpreted as frequency component at "$f_i - 2f_0$" [14]-[16], [19], [26], in which f_0 is the fundamental frequency. Hence, the sequence-domain admittance matrix including the MFC is defined as below [14], [16], [19]:

$$\begin{bmatrix} I_{p(f_i+f_0)} \\ I_{n(f_i-f_0)} \end{bmatrix} = \begin{bmatrix} Y_{pp(f_i)} & Y_{pn(f_i)} \\ Y_{np(f_i)} & Y_{nn(f_i)} \end{bmatrix} \begin{bmatrix} V_{p(f_i+f_0)} \\ V_{n(f_i-f_0)} \end{bmatrix} \quad (2)$$

In general, the frequency and sequence couplings can be created in a converter system due to the non-linear control, non-ideal DC-link, and asymmetry in a three-phase system [13]-[16], [23]-[26]. Further studies have attempted to address the couplings in the averaged multi-frequency models rigorously based on LTP [20], [24], multi-frequency linearization [27], and harmonic transfer matrix methods [28]-[30]. However, the inclusion of all couplings in a multi-frequency model would lead to a Multi-Input Multi-Output (MIMO) model with large matrices, very detailed equations and impractical stability studies [26], [30]-[32]. Reference [26] provides a quantitative method to acquire a reduced-order model of asymmetrical MMCs. Furthermore, reference [32] proposes an equivalent Single-Input Single-Output (SISO) transformation technique for LTP models of single-phase converters. However, these studies only consider the frequency couplings in the forms of "$f_i \pm kf_0$" (k=0,1,2,...) [23]-[32] using linearized averaged models. Thus, the non-linear convolution of non-ideal reference signal and non-ideal DC-link voltage in (1) is overlooked. Besides, the modelling and model-order reduction challenges in a MW-scale test environment have not been investigated abundantly. Reference [33] provides an excellent theoretical analysis for harmonic emissions by adopting Fourier transform on the switching model of a single-phase converter.

This paper hypothesizes that adopting the Fourier analysis on the responses of switching converters against small-signal perturbations can reveal any potential couplings and non-linearity and can be used to develop generic empirical models. Furthermore, this paper claims that the frequency couplings can exist in more general forms as linear combinations of multiples of the perturbation frequency and multiples of harmonics "$\pm mf_i \pm kf_0$" (k=0,1,2,..., and m=0,1,2,...), which should be considered in the MIMO models. A practical methodology for the identification of main couplings and generic multi-frequency model are proposed in sequence-domain to model the converter-connected REGs, i.e., PV converters and Type 4 WTs. A general theory for coupling patterns in switching converters has been presented in Part II. The proposed empirical modelling method and the main coupling selection criteria are proposed in Part III. Part IV demonstrates and summarizes the experimental verification of the proposed methodology by a 7MVA converter-based grid emulator.

II. Proposed General Theory for Repetitive Patterns of Frequency Couplings

In [33], an extensive Fourier analysis on the emissions from a switching model of a single-phase converter is provided. Accordingly, base-band, side-band and DC components are identified mathematically depending on the multi-frequency components in non-ideal $v_{abc(ref)}$ and v_{dc}. In this paper, the side-band and DC components are neglected since would be mostly eliminated by the converter filters. Considering a

single-phase converter, the interaction of f_{dc} component in the DC-link voltage with f_{hr} component in the modulation reference can generate the base-band components as [33]:

$$f_{dc} \circledast f_{hr} = \{f_{dc}, f_{hr}, f_0, f_{hr} \pm f_{dc}, f_0 \pm f_{dc}\} \quad (3)$$

where the sign "$\circledast$" depicts the convolution operation of modulation. Note that the positive and negative sequence characteristics of the components are not distinguished in (3) [33], and the analysis is only presented for a single-phase converter; yet it provides an excellent mathematical basis to study harmonic interactions in three-phase converters. It is expected that in a balanced three-phase converter, the frequency components of the DC-link (i.e., f_{dc}) would not appear on the AC side with the same frequencies [34].

A perturbation (f_h) flow into a converter-connected REG with positive and negative sequence control systems in dq-frame is illustrated in Fig. 1. The negative sequence control has been used widely to improve converters' dynamics against unbalances, voltage dips, and harmonics [28], [35]-[36]. Presence of a voltage perturbation with the frequency of f_h at the Point Of Connection (POC) to the converter leads to the emergence of ($f_h \mp f_0$) components in the voltage and current feed-backs of the $dq^{\pm}$-frame control [13]-[16], [28]. These components would add dynamics in the output signal of the PI-control of the current loop and the PLL angle (θ_{PLL}) [13], [28]. Later on, through the reverse transformation from $dq^{\pm}$ to abc-frame, the perturbation can emerge in the modulation reference signal with the frequency of f_h. The perturbation flow into the control system is likely for the frequencies below the cut-off frequency of digital and electrical filtering in converters.

Besides, low frequency perturbations can path through the converter's output filter and reach to the DC-link with frequency of "f_h-f_0" for positive sequence perturbation and "f_h+f_0" for negative sequence perturbation [34]. Similarly, the steady-state harmonics of "kf_0, (k=2,...)" in AC side can appear in the DC-link voltage as frequency of "$(k-1)f_0$" for positive sequence and "$(k+1)f_0$" for negative sequence harmonics. The coupling frequencies resulting from the perturbation flow into the control system and the DC-link voltage can be interpreted as repetitive patterns described below:

A. First stage coupling patterns

At the first stage, a perturbation leads to f_{hr}=f_h component in the control reference signal, and f_{dc}=$f_h \mp f_0$ components for small-signal and f_{dc}=$(k \mp 1)f_0$ for steady-state harmonics in the DC-link. According to (3), the first stage couplings are:

$$F_{ss(p)1} = (f_h - f_0) \circledast f_h = \{2f_0 - f_h, 2f_h - f_0, f_h, f_0\} \quad (4)$$

$$F_{ss(n)1} = (f_h + f_0) \circledast f_h = \{2f_0 + f_h, 2f_h + f_0, f_h, f_0\} \quad (5)$$

$$F_{hs(p)1} = (k-1)f_0 \circledast f_h = \{(k-2)f_0, f_h \pm (k-1)f_0, f_h, kf_0\} \quad (6)$$

$$F_{hs(n)1} = (k+1)f_0 \circledast f_h = \{(k+2)f_0, f_h \pm (k+1)f_0, f_h, kf_0\} \quad (7)$$

$F_{ss(p)1}$ and $F_{ss(n)1}$ provide the first stage small-signal coupling frequencies with positive and negative sequence perturbations. Fig. 1 indicates the perturbation flow into the converter (lined red boxes) and the first stage small-signal couplings (dashed blue box). Besides, F_{hss1} indicates the first group of coupling frequencies induced by the small-signal interactions in the positive and negative sequence (i.e., $F_{ss(p)1}$ and $F_{ss(n)1}$). $f_h \mp 2f_0$ frequencies are the dominant MFC components between positive and negative sequences with the original perturbation frequency "f_h" [16], [19], [34]. The rest of the frequency components are newly presented frequency couplings on the AC side of the converter.

B. Second stage coupling patterns

At the second stage, the newly induced frequencies into the AC side can flow into the controller and DC-link again. The second stage components are double attenuated and phase-shifted through the converter components and control systems. The interaction of the newly generated components in the DC-link and reference signal generates a group of new additional components as follows:

$$F_{ss(p)2} = (F_{ss(p)1} - f_0) \circledast F_{ss(p)1} = \{3f_h - 2f_0, 3f_0 - 2f_h, 4f_h - 3f_0, 4f_0 - 3f_h\} \quad (8)$$

$$F_{ss(n)2} = (F_{ss(n)1} + f_0) \circledast F_{ss(n)1} = \{3f_h + 2f_0, 3f_0, 3f_0 + 2f_h, 4f_h + 3f_0, 4f_0 + 3f_h, 4f_0 + f_h\} \quad (9)$$

$$F_{hs(p)2} = (F_{hs(p)1} + f_0) \circledast F_{hs(p)1} = \{(2k-1)f_0, , (2k-3)f_0, f_h + (2k-4)f_0, f_h \pm (k-3)f_0, 3f_0, (k+1)f_0 - f_h, 2kf_0 - f_h, f_h + (2k-3)f_0, f_h \pm (2k-2)f_0, f_h + (2k-4)f_0, 2f_h - kf_0, 2f_h + (k-2)f_0\} \quad (10)$$

$$F_{hs(n)2} = (F_{hs(n)1} + f_0) \circledast F_{hs(n)1} = \{(k+4)f_0, (2k+1)f_0, (2k+3)f_0, f_h - kf_0, f_h \pm (2k+4)f_0, f_h \pm (k+3)f_0, (k-1)f_0 - f_h, , f_h \pm (2k+2)f_0, f_h \pm (2k+4)f_0, 2f_h - kf_0, 2f_h + (k+2)f_0, 2f_h + (k+3)f_0\} \quad (11)$$

C. Repetitive loop of the new couplings

In general, the production of new couplings can continue in a repetitive loop of convolutions ("$\circledast$") to generate additional coupling components, as shown in Fig. 2. However, according to the conservation of energy Theorem, the multiplication of the frequency components into the coupling frequencies would be limited by the energy of the initial perturbation and additional potential energy from the converter-grid system [23], [28]. In addition, the digital or electrical filtering in the converter can attenuate or eliminate the high-frequency couplings [23], [28]. Therefore, the main coupling frequencies in response to the original perturbation can be considered only up to the first or second stages in (4)-(11).

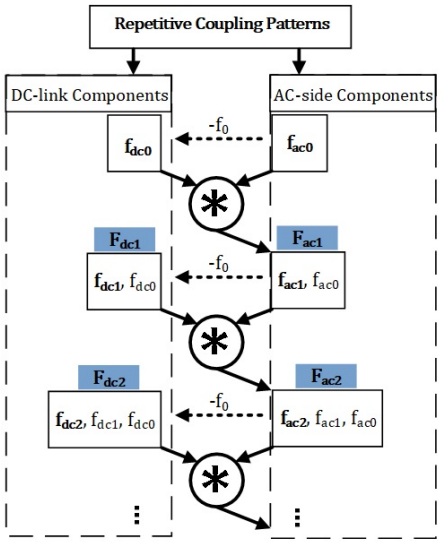

Fig. 2: Repetitive coupling patterns flowchart as convolution of multi-frequency components in DC-link and AC-side.

D. Mirror frequency patterns of couplings and sequence exchange

In a coupled converter system, each frequency coupling, given in (4)-(11), can cause a corresponding mirror frequency component with a "$2f_0$" frequency shift in the opposite sequence. For example, the positive sequence frequency coupling as "$2f_h - f_0$" can cause a corresponding MFC in the negative sequence at "$2f_h - 3f_0$".

Besides, the equivalent frequency of the coupling patterns can be negative. In this case, the conjugate of the frequency component can be presented in the opposite sequence with positive frequency expression [16], [19]. For instance, the positive sequence perturbation with frequency of "f_h" ($X_{p(f_h)}$), causes the MFC at "$f_h - 2f_0$" in the negative sequence ($X_{n(f_h-2f_0)}$). The sequence exchange of the sequence coupling can be expressed as follows [16], [19]:

$$X_{p(f_h)}, X_{n(f_h-2f_0)} = \begin{cases} X_{n(f_h-2f_0)}, & \text{if } f_h > 2f_0 \\ X^*_{p(2f_0-f_h)}, & \text{if} f_h < 2f_0 \\ X_{(0)}, (DC\ value) & \text{if} f_h = 2f_0 \end{cases} \quad (12)$$

where "X" refers to any electrical variable including voltage, current, admittance, or impedance. Therefore, in the range of "$f_h < 2f_0$", the negative sequence coupling ($X_{n(f_h-2f_0)}$) would be observed in the positive sequence in conjugated form ($X^*_{p(2f_0-f_h)}$). Similar to (12), the sequence exchange of different couplings can be observed in a converter response. The coupling patterns are used for main couplings identification and generic multi-frequency modelling in Part III.

III. Proposed Generic Multi-frequency Modelling Methodology

According to the descriptions in Part II, the interaction of a perturbation with a converter system generates frequency and sequence couplings. Hence, the accuracy of multi-frequency models depends on their ability to address the couplings and the converter dynamics. In this part of the paper, a generic multi-frequency model is proposed. Later on, a methodology for couplings identification and selection criteria are provided.

A. Proposed Generic Multi-frequency Model Considering Couplings

A generic multi-frequency model for the frequency of "f_i" can be illustrated as a Norton equivalent or Thevenin equivalent for positive and negative sequences [7]. The proposed generic multi-frequency model for converters as a Norton equivalent is presented as follows:

$$I_{p(f_i+f_0)} = I_{p0(f_i+f_0)} + \sum_{j=1}^{k} Y_{pp(f_i,f_j)} V_{p(f_j+f_0)} + \sum_{j=1}^{k} Y_{pn(f_i,f_j)} V_{n(f_j-f_0)} \quad (13)$$

$$I_{n(f_i-f_0)} = I_{n0(f_i-f_0)} + \sum_{j=1}^{k} Y_{np(f_i,f_j)} V_{p(f_j+f_0)} + \sum_{j=1}^{k} Y_{nn(f_i,f_j)} V_{n(f_j-f_0)} \quad (14)$$

Considering a positive sequence perturbation at "$f_i + f_0$", the self-excitation response is considered as "$Ypp(f_i, f_i)$". The potential frequency couplings are included in the forms of "$Ypp(f_i, f_j)$" (j$\neq$ i). In addition, the Mirror Frequency Coupling (MFC) is located at "$Ypn(f_i, f_i)$" and the sequence coupling is addressed in "$Ypn(f_i, f_i + 2f_0)$". Similarly, considering a negative sequence perturbation at "$f_i - f_0$", the frequency couplings as "$Ynn(f_i, f_j)$" (j$\neq$ i), the MFC component at "$Ynp(f_i, f_i)$", and the sequence coupling at "$Ynp(f_i - 2f_0, f_i)$" are addressed. The initial values "$I_{p0(f_i+f_0)}$" and "$I_{n0(f_i-f_0)}$" indicate the initial emission of the converter. The initial emissions can be used for power quality calculations. Note that there is a frequency shift of "$-2f_0$" between the positive and negative sequence perturbations similar to (2) [13], [14], [16], [19]. In fact, the proposed model in (13)-(14) is an extended form of (2) to address the main couplings. The equations (13)-(14) can be illustrated in a general matrix form for k number of frequencies as follows:

$$\begin{bmatrix} I_p^1 \\ I_p^2 \\ \vdots \\ I_p^k \end{bmatrix} = \begin{bmatrix} I_{p0}^1 \\ I_{p0}^2 \\ \vdots \\ I_{p0}^k \end{bmatrix} + \begin{bmatrix} Y_{pp}^{1\,1} & Y_{2p}^{1\,2} & \dots & Y_{ip}^{1\,k} \\ Y_{1p}^{2\,1} & Y_{pp}^{2} & \dots & Y_{ip}^{2\,k} \\ \vdots & \vdots & \dots & \vdots \\ Y_{kp}^{k\,1} & Y_{ip}^{k\,2} & \dots & Y_{pp}^{k} \end{bmatrix} \begin{bmatrix} V_p^1 \\ V_p^2 \\ \vdots \\ V_p^k \end{bmatrix} + \begin{bmatrix} Y_{pn}^{1\,1} & Y_{pn}^{1\,2} & \dots & Y_{pn}^{1\,k} \\ Y_{pn}^{2\,1} & Y_{pn}^{2\,2} & \dots & Y_{pn}^{2\,k} \\ \vdots & \vdots & \dots & \vdots \\ Y_{pn}^{k\,1} & Y_{pn}^{k\,2} & \dots & Y_{pn}^{k\,k} \end{bmatrix} \begin{bmatrix} V_n^1 \\ V_n^2 \\ \vdots \\ V_n^k \end{bmatrix} \quad (15)$$

$$I_{p(f+f_0)} = I_{p0(f+f_0)} + Y_{pp} V_{p(f+f_0)} + Y_{pn} V_{n(f-f_0)} \quad (16)$$

Note that (16) is a simplified illustration of (15). Accordingly, the diagonal arrays of Y_{pp} represent the self-excitation admittance components ($Y_{pp}^{i\ i}$). Moreover, the diagonal components of Y_{pn} refer to the MFCs and the arrays with similar frequencies to $I_{p(f+f_0)}$ (i.e., "$Y_{pn(f,f+2f_0)}$") are the sequence couplings. The rest of the arrays in Y_{pp} and Y_{pn} are related to the potential frequency couplings, corresponding MFCs and sequence couplings, and additional design-related couplings. Similarly, the negative sequence current response of the converter can be depicted as follows:

$$\begin{bmatrix} I_n^1 \\ I_n^2 \\ \vdots \\ I_n^k \end{bmatrix} = \begin{bmatrix} I_{n0}^1 \\ I_{n0}^2 \\ \vdots \\ I_{n0}^k \end{bmatrix} + \begin{bmatrix} Y_{nn}^{1\ 1} & Y_{2n}^{1\ 2} & \dots & Y_{kn}^{1\ k} \\ Y_{1p}^{2\ 1} & Y_{nn}^{2\ 2} & \dots & Y_{kn}^{2\ k} \\ \vdots & \vdots & \dots & \vdots \\ Y_{kn}^{k\ 1} & Y_{in}^{i\ 2} & \dots & Y_{nn}^{k\ k} \end{bmatrix} \begin{bmatrix} V_n^1 \\ V_n^2 \\ \vdots \\ V_n^k \end{bmatrix} + \begin{bmatrix} Y_{np}^{1\ 1} & Y_{np}^{1\ 2} & \dots & Y_{np}^{1\ k} \\ Y_{np}^{2\ 1} & Y_{np}^{2\ 2} & \dots & Y_{np}^{2\ k} \\ \vdots & \vdots & \dots & \vdots \\ Y_{np}^{k\ 1} & Y_{np}^{k\ 2} & \dots & Y_{np}^{k\ k} \end{bmatrix} \begin{bmatrix} V_p^1 \\ V_p^2 \\ \vdots \\ V_p^k \end{bmatrix} \quad (17)$$

$$I_{n(f-f_0)} = I_{n0(f-f_0)} + Y_{np}V_{p(f+f_0)} + Y_{nn}V_{n(f-f_0)} \quad (18)$$

Similarly, the diagonal arrays of Y_{nn} (i.e., $Y_{nn}^{i\ i}$) are self-excitation admittance. In addition, the diagonal arrays of Y_{np} depicts the mirror frequency coupling components and the sequence couplings are located at $Y_{np(f-2f_0,f)}$. The rest of the arrays in Y_{nn} and Y_{np} are related to the potential frequency couplings, corresponding sequence couplings, and additional design-related couplings.

Note that the positive sequence voltage and current vectors have "$+2f_0$" frequency shifts from the negative sequence vectors. The admittance matrices provide the sensitivity of the output currents to the voltage perturbations at POC. Therefore, the proposed model parameters can be calculated using small-signal perturbation tests. Besides, the Thevenin illustration of the generic model can be illustrated as follows:

$$\begin{aligned} V_{p(f_p+f_0)} &= Z_{pp}I_{p(f_p+f_0)} + Z_{pn}I_{n(f_p-f_0)} + V_{p0(f_p+f_0)} \\ V_{n(f_p-f_0)} &= Z_{np}I_{p(f_p+f_0)} + Z_{nn}I_{n(f_p-f_0)} + V_{n0(f_p-f_0)} \end{aligned} \quad (19)$$

Similarly, the impedance matrices can be interpreted as the output voltage sensitivity to current perturbations at POC. The proposed methodology for the derivation of the admittance or impedance matrices is described in the next section. Note that the application of the proposed generic model in harmonic stability studies at the system level is out of the scope of this paper. Nevertheless, since the method provides a MIMO model, one approach would be applying the generalized Nyquist criterion for the harmonic stability study of network systems [14], [28]. Besides, the stochasticity of renewable energy sources (i.e., wind or solar energy) might indirectly affect the multi-frequency models through the output power of the converters. The evaluation of such effects is out of the scope of this paper. This simplification has been applied in [19]-[20], [24]-[28] as well.

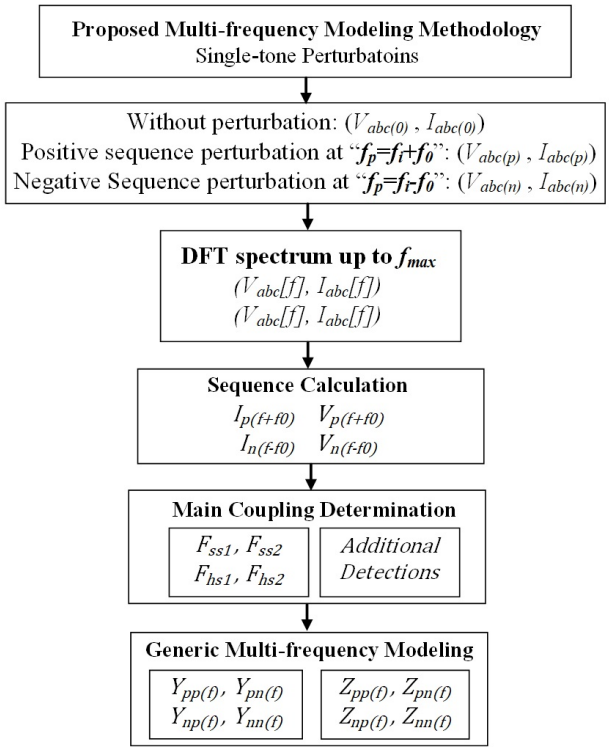

Fig. 3: Proposed generic multi-frequency modelling methodology based on empirical perturbations and main couplings identification.

B. Multi-frequency modelling Methodology based on perturbation tests

As explained in Part II, a repetitive loop for the couplings generation can exist in a converter. Analytical modelling and identifying the couplings can be challenging due to the non-linearity and complexities in a converter design. Therefore, this paper proposes a methodology to identify the main coupling patterns using empirical tests. Inspired by the harmonic linearization technique, the voltage or current perturbation tests have been used for the multi-frequency model validation purposes [13], [16], [19]-[22], [24]. This paper proposes a methodology to extend the application of the sequence-domain perturbation tests to identify the main couplings, as shown in Fig. 3. Accordingly, single frequency (single-tone) perturbations in positive and negative sequences are injected. Then, for each perturbation test, the Discrete Fourier Transform (DFT) of the measured voltages and currents at the POC (V_{poc}, I_{poc} in Fig. 1) are calculated for a range of frequencies up to f_{max}. Later on, the calculated DFT components are transformed to the sequence domain. According to Fig. 3, three different measurement data matrices should be prepared in sequence domain: 1) Normal operation without any perturbation ($V_{p(0)}, V_{n(0)}, I_{p(0)}, I_{n(0)}$), 2) Positive sequence perturbation tests at frequencies of "$f_i + f_0$" ($V_{p(p)}, V_{n(p)}, I_{p(p)}, I_{n(p)}$), and 3) Negative sequence perturbation tests at frequencies of "$f_i - f_0$" ($V_{p(n)}, V_{n(n)}, I_{p(n)}, I_{n(n)}$). The three groups of data can be substituted in equations (16) and (18) and simplified by subtracting the initial values as below:

$$\begin{bmatrix} V_{p(p)}-V_{p(0)} & V_{n(p)}-V_{n(0)} \\ V_{p(n)}-V_{p(0)} & V_{n(n)}-V_{n(0)} \end{bmatrix} \begin{bmatrix} Y_{pp} \\ Y_{pn} \end{bmatrix} = \begin{bmatrix} I_{p(p)}-I_{p(0)} \\ I_{p(n)}-I_{p(0)} \end{bmatrix} \\ \begin{bmatrix} V_{p(p)}-V_{p(0)} & V_{n(p)}-V_{n(0)} \\ V_{p(n)}-V_{p(0)} & V_{n(n)}-V_{n(0)} \end{bmatrix} \begin{bmatrix} Y_{np} \\ Y_{nn} \end{bmatrix} = \begin{bmatrix} I_{n(p)}-I_{n(0)} \\ I_{n(n)}-I_{n(0)} \end{bmatrix} \tag{20}$$

This way, the effects of the initial emissions on the calculation results can be eliminated. The emissions at normal operation can be emitted by converters or AC grid, which are neglected in the model calculations in [16], [19], [22], [24]. The initial emissions may not be significant for the stability studies, yet crucial for accurate experimental model calculations and validations. Hereafter, the prefix "Δ" indicates the subtraction of the initial emissions. Solving (20) obtains the admittance matrices:

$$\begin{aligned} Y_{pp} =& (\Delta I_{p(p)}\Delta V_{n(n)} - \Delta I_{p(n)}\Delta V_{n(p)}) \times D^{-1} \\ Y_{pn} =& (\Delta I_{p(n)}\Delta V_{p(p)} - \Delta I_{p(p)}\Delta V_{p(n)}) \times D^{-1} \\ Y_{nn} =& (\Delta I_{n(n)}\Delta V_{p(p)} - \Delta I_{n(p)}\Delta V_{p(n)}) \times D^{-1} \\ Y_{np} =& (\Delta I_{n(p)}\Delta V_{n(n)} - \Delta I_{n(n)}\Delta V_{n(p)}) \times D^{-1} \\ D =& \Delta V_{p(p)}\Delta V_{n(n)} - \Delta V_{p(n)}\Delta V_{n(p)} \end{aligned} \tag{21}$$

Furthermore, the initial current values can be calculated afterwards using (16), (18) and (21) as follows:

$$\begin{aligned} I_{p0} &= I_{p(0)} - Y_{pp}V_{p(0)} - Y_{pn}V_{n(0)} \\ I_{n0} &= I_{n(0)} - Y_{np}V_{p(0)} - Y_{nn}V_{n(0)} \end{aligned} \tag{22}$$

Moreover, the impedance matrices of a Thevenin equivalent in (19) can be determined by its dual Norton model in (16) and (18) as follows:

$$\begin{aligned} Z_{pp} &= \frac{Y_{nn}}{Y_{pp}Y_{nn} - Y_{pn}Y_{np}} \\ Z_{pn} &= \frac{-Y_{pn}}{Y_{pp}Y_{nn} - Y_{pn}Y_{np}} \\ Z_{nn} &= \frac{Y_{pp}}{Y_{pp}Y_{nn} - Y_{pn}Y_{np}} \\ Z_{np} &= \frac{-Y_{np}}{Y_{pp}Y_{nn} - Y_{pn}Y_{np}} \end{aligned} \tag{23}$$

The impedances and admittances in (23) are "k×k" matrices. Therefore, the effects of the couplings are included through the matrix calculations. The criteria for the selection of strong couplings are described in the next section.

C. Main couplings selection criteria

The accuracy of the extracted multi-frequency model depends on the number of the included couplings in the model. Thus, it is a trade-off between the accuracy and complexity of the model in selecting the minimum number of arrays in the admittance or impedance matrices. The main couplings selection criteria are proposed as follows:

1) Coupling patterns: As shown in Fig. 3, the first two groups of coupling frequencies to be checked are given in equations (4)-(11). Relatively high values in the coupling patterns should be addressed in the multi-frequency model (equations (16) and (18)). It should be noted that there could be a group of couplings that are depending on the converter's specific design and could only be detected by perturbation tests.

2) Harmonic emission standards: The maximum eligible distortion limits for AC grids and converters can be used based on relevant international standards. For instance, the harmonic emission limits for the connection of distorting installations to different power systems are given in IEC 61000-3-6 [37]. The maximum eligible harmonic voltage distortion of AC grids can be used to determine proper amplitudes of voltage perturbations, and the converter's response current can be assessed. Note that in the IEC 61000-3-6, the values are provided only for harmonics (i.e., kf_0, k=2,3,...), and the harmonic spectrum is calculated with 5Hz resolution and summation of the near inter-harmonics (i.e., non-integer multiples of the fundamental frequency) with the harmonics in calculations [37]-[38]. Therefore, a safe margin for perturbation amplitudes would be less than the given emission limits in IEC-61000-3-6. Furthermore, special attention should be considered for the low-frequency range ($f_p < 2f_0$) because the current responses would be very high for even small amplitudes of voltage perturbations. A limit of 0.2% per-unit (pu) is recommended for voltage inter-harmonics below "$2f_0$" in [37]. The couplings that do not affect the converter response and are significantly smaller than maximum current or voltage emission limits (e.g., 100 times less) could be neglected.

3) Measurement equipment accuracy: The resolution and accuracy of the measurement equipment are determinants of coupling detection and model validation procedure. In IEC 61000-4-7 standard [38], it is recommended to utilize Class I measurement instruments for high precision applications. Accordingly, Class I instruments should have a maximum error of "$\pm 0.05\%$ pu" for voltage measurements and "$\pm 0.15\%$ pu" for current measurements in the small-signal range [38]. Therefore, the measurement data near the maximum errors should not be considered in the model validation procedure. However, the subtractions in equations (20)-(21) can cancel out the common-mode noises on the measured data [38]-[39].

4) Admittance or impedance arrays comparison: Another practical criterion can be comparing the amplitude of the coupling arrays in the admittance or impedance matrices. A minimum threshold for admittance arrays (e.g., in the range of 0.05-0.01 pu) and a maximum threshold for impedance arrays (e.g., in the range of 20-100 pu) can be chosen to simplify the model while not compromising the model accuracy.

IV. Experimental Verification of the Proposed Methodology

The experimental single-tone voltage perturbation tests are performed by a 7MVA/ 13.8kV grid emulator at National Renewable Energy Laboratory (NREL), USA [11], [21], [40]. We have illustrated the simulation results of perturbation

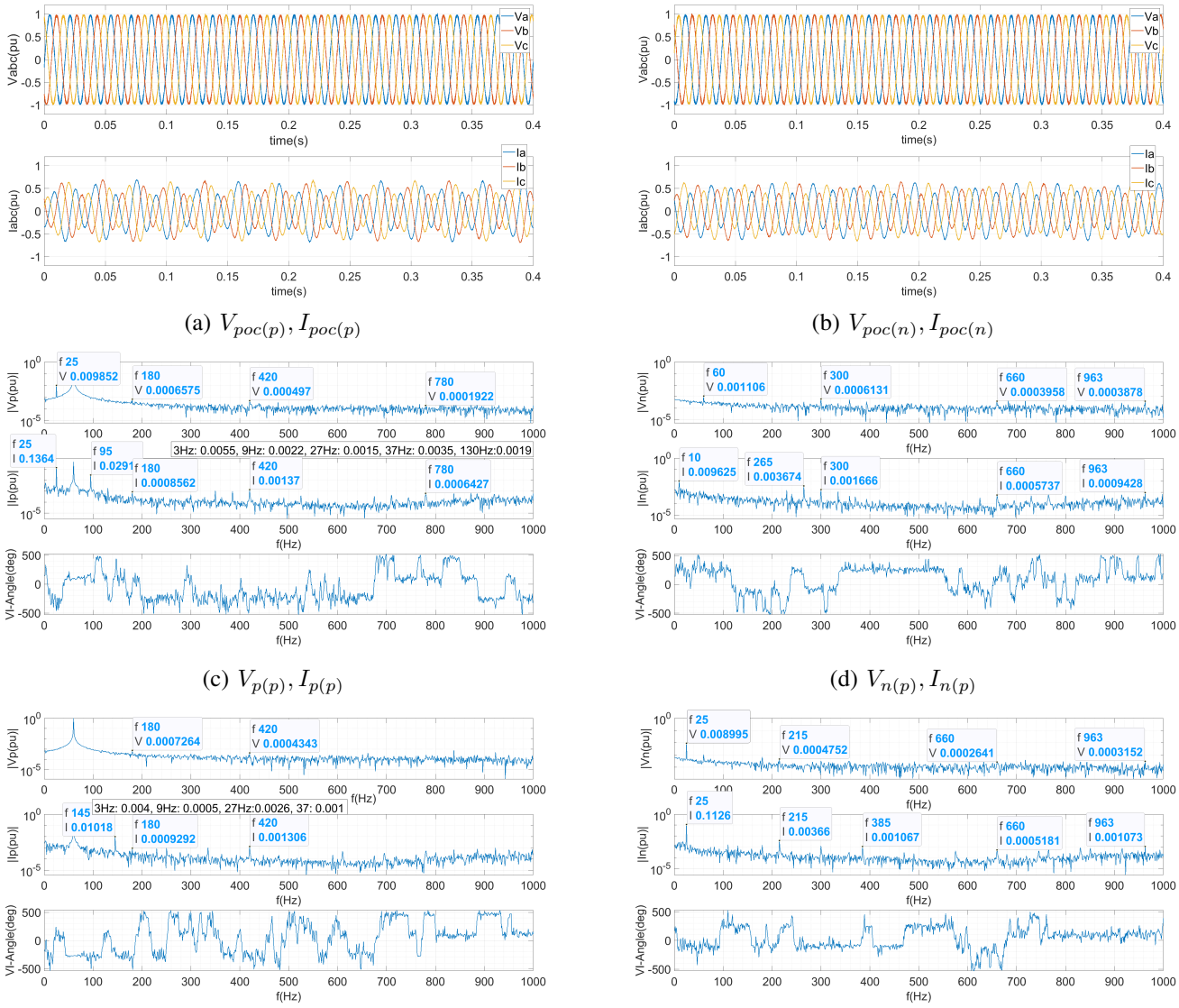

(a) $V_{poc(p)}, I_{poc(p)}$ (b) $V_{poc(n)}, I_{poc(n)}$

(c) $V_{p(p)}, I_{p(p)}$ (d) $V_{n(p)}, I_{n(p)}$

(e) $V_{p(n)}, I_{p(n)}$ (f) $V_{n(n)}, I_{n(n)}$

Fig. 4: Experimental test results with logarithmic axes for positive and negative sequence single-tone perturbations at 25Hz: (a,b) Time-domain voltages and currents, (c,d) DFT for positive sequence perturbation, (e,f) DFT for negative sequence perturbation.

tests on Type 4 and Type 3 WTs in reference [41]. In this paper, the experimental perturbation tests are performed on a balanced three-phase 2MVA PV converter with the fundamental frequency of 60Hz. The three-phase voltage and currents are measured using data acquisition modules with 50kS/s speed and 18bit resolution [11], [21]. According to the proposed methodology in Fig. 3, the Discrete Fourier Transform (DFT) of the measured data is calculated with a 1-second DFT window to achieve a 1Hz resolution. The DFT calculation method is provided in IEC 61000-4-7 [38]. The voltage perturbation tests are used for verification of the proposed methodology as follows:

A. One single-tone voltage perturbation analysis

In this case study, one positive and one negative sequence single-tone voltage perturbation test results for 25Hz are illustrated in Fig. 4. Accordingly, Fig. 4.(a)-(b) demonstrate time-domain three-phase voltages and currents at the POC during the positive and negative sequence 25Hz perturbations, respectively. As it is shown, 1% pu perturbations do not affect the AC voltages, while they cause relatively high distortions on the output currents (i.e., $I_{poc(p)}$ and $I_{poc(n)}$).

Fig. 4.(c)-(d) represent the harmonic spectrum of the positive and negative sequence voltages, currents, and the phase angles between them with logarithmic Y-axes. Accordingly, considerable couplings exist in 95Hz (equals to $2f_0 - f_p$ in (4) or the mirror frequency coupling) and 130Hz (equals to $3f_0 - 2f_p$ in (8)) at the positive sequence current ($I_{p(p)}$), and 10Hz (equals to $f_0 - 2f_p$ in (4)) and 265Hz (equals to $4f_0 + f_p$ in (6)) at the negative sequence ($I_{n(p)}$). Furthermore, the steady-state harmonics of 180Hz, 420Hz and 780Hz (i.e., 3rd, 7th, and 13th order harmonics) in the positive sequence, as

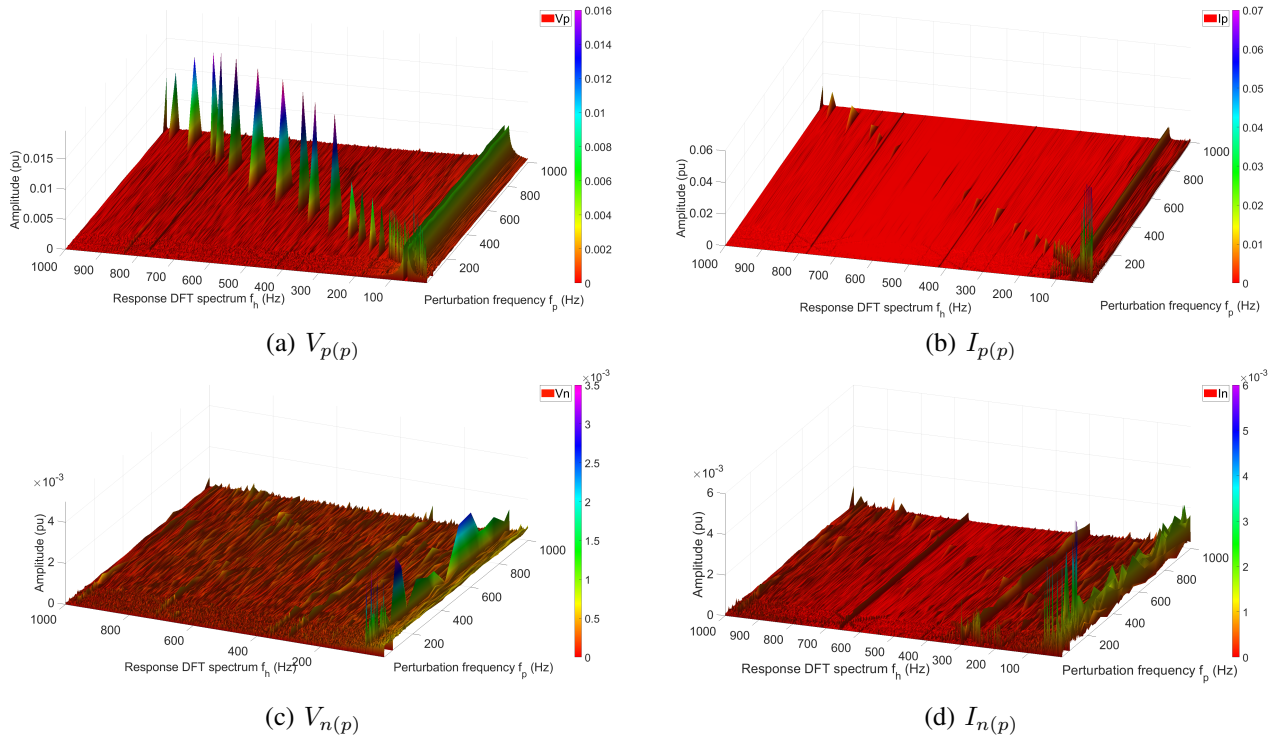

(a) $V_{p(p)}$ (b) $I_{p(p)}$

(c) $V_{n(p)}$ (d) $I_{n(p)}$

Fig. 5: DFT spectrum of the positive and negative sequence voltage and current (excluding the fundamental component) for experimental positive sequence voltage perturbation tests on a 2MVA PV converter.

well as 60Hz, 300Hz, and 660Hz (1st, 5th, and 11th orders) in the negative sequence are detected. Similarly, Fig. 4.(e)-(f) present the voltage and current spectrum in response to a negative sequence 25Hz voltage perturbation. Accordingly, a considerable coupling at 145Hz (equals to $2f_0 + f_p$ in (5)) in positive sequence and 215Hz (equals to $4f_0 - f_p$ in (11)), 385Hz (equals to $6f_0 + f_p$ in (7)) are observed in the negative sequence. Note that small amounts of frequency components such as 3Hz, 9Hz, 27Hz, 37Hz, and 963Hz are visible in the test results, which can be considered as the consequences of the non-ideal single-tone perturbations with a grid emulator. The evaluation of such effects is out of the scope of this paper.

B. Single-tone voltage perturbation tests for coupling identification and multi-frequency modelling

This section presents a group of single-tone voltage perturbation tests for positive and negative sequences from 3Hz up to 1kHz. The experimental results for the positive sequence perturbations are demonstrated in Three-Dimensional (3D) plots in Fig. 5. Accordingly, the f_p-axis determines the frequency of single-tone voltage perturbations, f_h-axis illustrates the frequency of the converter response at the POC. Furthermore, the Z-axis gives the amplitude of the corresponding DFT calculations. The perturbations have been implemented for a limited number of frequencies from 3Hz up to 1kHz. Thus, the plots are in discrete form. Similar 3D plots for the negative sequence perturbations are omitted.

In the illustrated 3D plots in Fig. 5-(a)-(b), the main diagonal lines imply the converter response (f_h) to the perturbations (f_p) at the same frequency and can be called "self-frequency excitation ($f_p = f_h$)". The diagonal lines in Fig. 5-(c)-(d) can depict the sequence couplings, which have not been detected in these experiments. Furthermore, the lines parallel with the f_p-axis represent the groups of frequency components independent of the perturbation frequency i.e., steady-state harmonics. The rest of the components reveal the frequency couplings and their corresponding MFC couplings. Note that the amplitudes of currents in sub-synchronous frequencies ($f_h < 60$Hz) are relatively high. The amplitude of the voltage perturbations is chosen 0.01 pu in the sub-synchronous range to limit the current response amplitudes. The amplitude of voltage perturbations for higher frequencies is chosen 0.02 pu. The overall view of plots in Fig. 5 depicts that the strong couplings are limited to the low-frequency range of $f_h <$ 400Hz and $f_p <$ 150Hz (except for the lines around 7th and 13th-order harmonics in Fig. 5.(a)-(b)). Therefore, a detailed analysis for low frequencies is presented in the next section.

C. Detailed demonstration of results in low-frequency range

The results of the positive and negative sequence perturbation tests in the ranges of $f_h <$ 400Hz and $f_p <$ 150Hz are illustrated in Fig. 6. The minimum level of 0.05% pu is chosen in the plots to emphasize the considerable amplitudes. In fact, Fig. 6 is a top-view (f_p-axis versus f_h-axis) of Fig. 5 in the specified frequency range, which is explained as follows:

1) $V_{p(p)}$,$I_{p(p)}$: According to Fig. 6.(a)-(b), the self-frequency excitation components have relatively high current amplitudes ($f_h = f_p$). Besides, a group of frequencies (58-62 Hz) are independent of the perturbation frequencies as

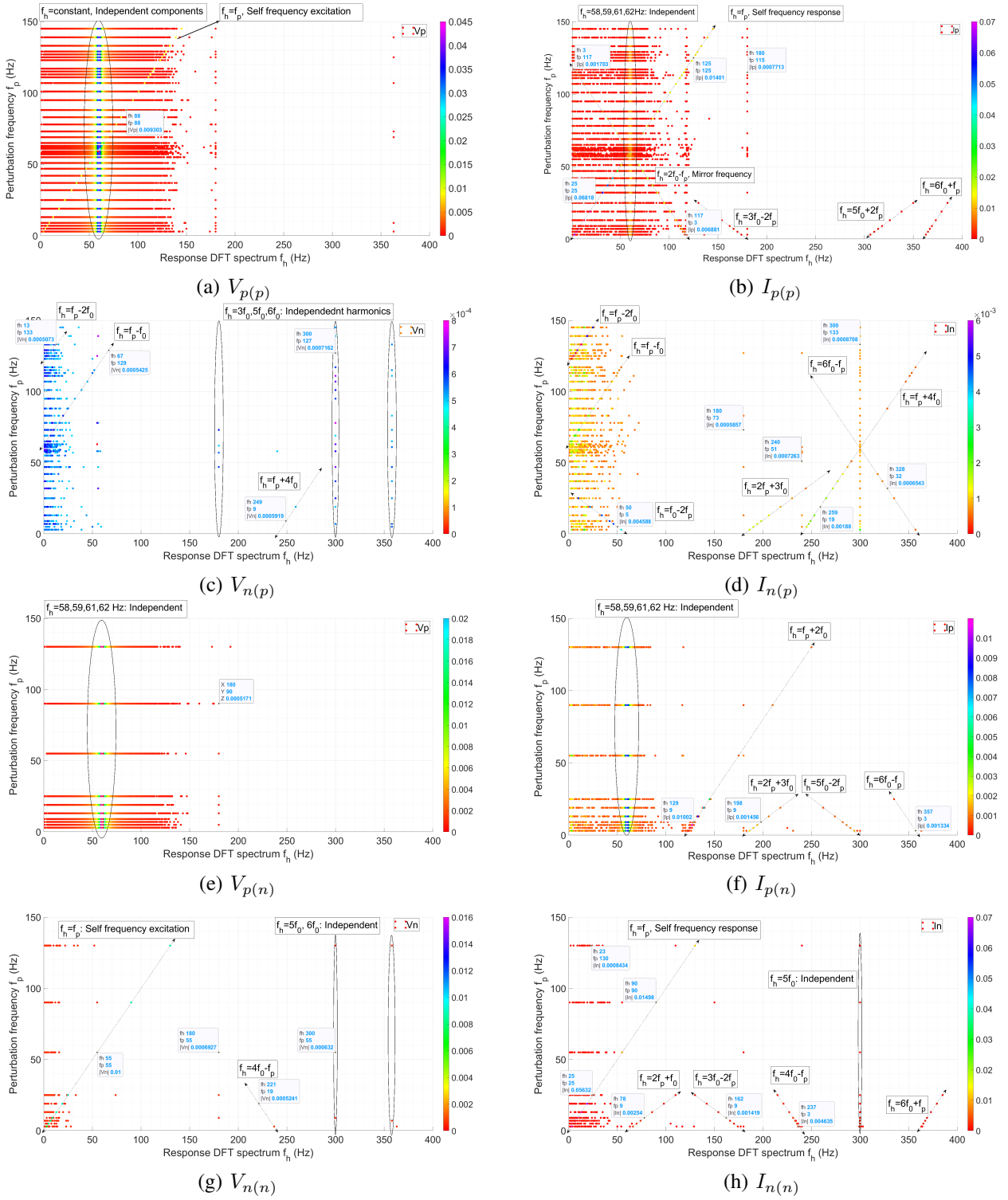

Fig. 6: Coupling demonstration of the experimental positive and negative sequence perturbations for values above 0.05% pu.

parallel lines with f_p-axis. These small independent lines are the side-band components of the fundamental frequency and are emitted due to the non-ideal voltage source behaviour of the grid emulator. The frequency couplings are not visible in Fig. 6.(b) due to the dominant amplitudes of the MFC components. As shown in Fig. 5.(b)-(d), the interactions with 7th and 13th-order harmonics leads to: $F_{hsp(p)} = \{f_p + 6f_0, 8f_0 - f_p, f_p + 12f_0 14f_0 - f_p\}$, $F_{hsn(p)} = \{f_p + 4f_0, 6f_0 - f_p, f_p + 10f_0, 12f_0 - f_p\}$.

Note that the couplings with 7th and 13th harmonics in positive sequence ($F_{hsp(p)}$) have corresponding mirror frequency couplings with 5th and 11th harmonics in $F_{hsn(p)}$.

2) $V_{n(p)}$,$I_{n(p)}$: Similarly, a number of independent frequency components {60, 180, 300, 360Hz} (or 1st, 3rd,

Perturbation	Couplings in the perturbation sequence	Corresponding MFCs in the opposite sequence
$V_{p(p)}$	$f_p, 2f_0-f_p(for f_p<2f_0), f_p+f_0, 2f_p-f_0, 2f_p+5f_0, f_p+6f_0, 8f_0-f_p, f_p+12f_0, 14f_0-f_p$	$f_p-2f_0(for f_p>2f_0), f_p-f_0, 2f_p-3f_0, 2f_p+3f_0, f_p+4f_0, 6f_0-f_p, f_p+10f_0, 12f_0-f_p$
$V_{n(n)}$	$f_p, f_p-f_0, 2f_p-3f_0, 2f_p+3f_0, f_p+4f_0, 6f_0-f_p, f_p+10f_0, 12f_0-f_p$	$f_p+2f_0, f_p+f_0, 2f_p-f_0, 2f_p+5f_0, f_p+6f_0, 8f_0-f_p, f_p+12f_0, 14f_0-f_p$

TABLE I: Summary of observed couplings at the perturbation sequence and corresponding MFCs in the opposite sequence.

5th and 6th harmonics) are observed in the negative sequence. Moreover, the coupling frequencies are highlighted with double-arrow lines are interpreted as: $F_{ssn(p)} = \{f_p - 2f_0, f_0 - 2f_p, 2f_p + 3f_0\}$, $F_{hsn(p)} = \{f_p + 4f_0, 6f_0 - f_p, f_p - f_0\}$, which $F_{ssn(p)}$ and $F_{hsn(p)}$ refer to small-signal and harmonics interactions as (4)-(11).

3) $V_{p(n)}$,$I_{p(n)}$: The frequency of negative sequence perturbations have "$-2f_0$" shift from the positive sequence perturbations. As explained in (12), the mirror frequency perturbations for $f_h < 120Hz$ are presented in the positive sequence with a conjugation operation. Thus, for this range, the tests are realized in the positive sequence, as shown in Fig. 6.(a)-(b). While the tests for $f_h > 120Hz$ are performed in the negative sequence. The coupling patterns in the negative sequence are detectable from Fig.6.(e)-(h). Strong couplings are observed in the current response $I_{p(n)}$ as: $F_{ssp(n)} = \{f_p + 2f_0, 2f_p + 3f_0, 5f_0 - 2f_p\}$ and $F_{hsp(n)} = \{6f_0 - f_p\}$.

4) $V_{n(n)}$,$I_{n(n)}$: The self-frequency excitation lines ($f_h = f_p$) are illustrated in Fig.6.(g)-(h). In addition, strong couplings in current are visible as: $F_{ssn(n)} = \{2f_p + f_0, 3f_0 - 2f_p\}$, $F_{hsn(n)} = \{4f_0 - f_p\}$. Note that the couplings in the negative sequence have only "$-2f_0 = -120Hz$" frequency shifts from the couplings in the positive sequence in previous section (Part IV.C.3). This finding proves the fact that the frequency couplings in one sequence can cause corresponding mirror frequency couplings in the opposite sequence.

D. Summary of the findings from the experimental results

1) The amplitude of the current response has very high values for the sub-synchronous frequency range, while it is small for high frequencies. In this paper, the safe margins for the voltage perturbations are chosen as less than 1% pu (i.e., $\Delta V_{p(p)} < 1\%pu$ and $\Delta V_{n(n)} < 1\%pu$) for the low (less than $2f_0$) and less than 2% pu for the high frequency perturbations.

2) Fig. 6 is demonstrated for the values above 0.05%. Despite the effectiveness of this noise level consideration for high frequencies, there are still lots of components in the low-frequency range that can be eliminated. Therefore, it is proposed to apply different noise levels for different frequency ranges to achieve a better coupling identification. One way would be to formulate the minimum level as a function of frequency (f_h); however, it has not been necessary for the test results in this paper. Therefore, 0.1% pu noise level is applied for "$f_h < 150Hz$" (within the PV converter control bandwidth) and 0.05% pu for higher frequencies.

3) The observed couplings and the corresponding MFCs above noise level of 0.05% are summarized in Table I. Accordingly, the detected coupling patterns have been predicted in the first two groups of the proposed theory in (4)-(11).

The small-signal couplings are mostly observed in the limited range of perturbation frequencies ($f_p < 150Hz$) and response frequencies ($f_h < 400Hz$). Besides, couplings with 7th and 13th steady-state harmonics in positive sequence (i. e., $f_p + 6f_0$ and $f_p + 12f_0$), and 5th and 11th harmonics in negative sequence (i. e., $6f_0 - f_p$ and $12f_0 - f_0$) are identified as in (4)-(7). To address the couplings in a model as (15)-(18), the patterns in Table I should be reformulated based on f_p as:

$$f_{p(p)} = \{f_h, f_h - f_0, (f_h + f_0)/2, (f_h - 5f_0)/2, f_h - 6f_0, 8f_0 - f_h, f_h - 12f_0, 14f_0 - f_h\} \quad (24)$$

$$f_{p(n)} = \{f_h, f_h + f_0, 2f_h + 3f_0, (f_h - 3f_0)/2, f_h - 4f_0, 6f_0 - f_h, f_h - 10f_0, 12f_0 - f_h\} \quad (25)$$

Later on, using (16), (18), and (24)-(25), the generic multi-frequency model for the tested PV converter can be defined:

$$\begin{bmatrix}\Delta I_{p(f_i+f_0)}\\ \Delta I_{n(f_i-f_0)}\end{bmatrix} = \begin{bmatrix}Y_{pp}\ Y_{pn}\\ Y_{np}\ Y_{nn}\end{bmatrix} \begin{bmatrix}\Delta V_{p(f_i+f_0)}\\ \Delta V_{p(f_i)}\\ \Delta V_{p((f_i+2f_0)/2)}\\ \Delta V_{p((f_i-4f_0)/2)}\\ \Delta V_{p(f_i-5f_0)}\\ \Delta V_{p(7f_0-f_i)}\\ \Delta V_{p(f_i-11f_0)}\\ \Delta V_{p(13f_0-f_i)}\\ \Delta V_{n(f_i+3f_0)}\\ \Delta V_{n(f_i+2f_0)}\\ \Delta V_{n((f_i+4f_0)/2)}\\ \Delta V_{n((f_i-2f_0)/2)}\\ \Delta V_{n(f_i-3f_0)}\\ \Delta V_{n(5f_0-f_i)}\\ \Delta V_{n(f_i-9f_0)}\\ \Delta V_{n(11f_0-f_i)}\end{bmatrix} \quad (26)$$

4) Case study: To evaluate the effectiveness of the proposed model in (26), the output current of 650Hz positive sequence perturbation test is reconstructed. The reconstruction is accomplished by multiplicating its voltage measurement data with the calculated admittance model [28]. The comparison of the measured data with the reconstructed values is presented with logarithmic axis in Fig. 7. Due to the limited number of perturbation tests, the reconstructed current response has only a few points illustrated with star signs "*". In addition, two different minimum levels are suggested for low frequency

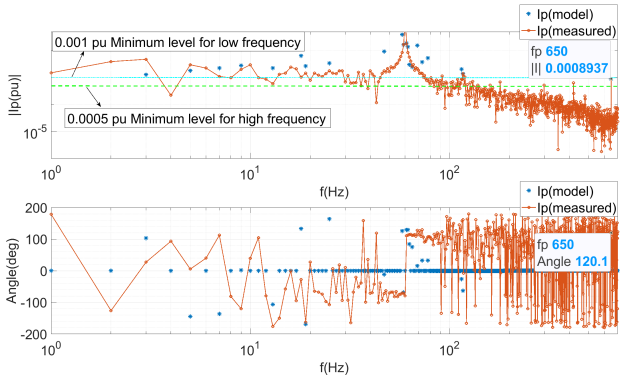

Fig. 7: Response current reconstruction case study for 650Hz perturbation test using the proposed model.

(0.1% pu for below 150Hz) and high-frequency ranges (0.05% pu for higher than 150 Hz). The logarithmic axes in Fig. 7 highlights the importance of different minimum levels for coupling identification, where even the current response at 650Hz is between the two levels. Besides, some of the points resemble the measured current response perfectly, while some other points still have errors. Such errors highlight the necessity of couplings inclusion in the low-frequency range. To reconstruct the current response at one specific frequency by the proposed model in (26), one perturbation test is required at that specific frequency. Since the coupling pattern of "$f_{p(p)} = (f_h + f_0)/2$" in (26) is considerable for low-frequencies (Fig. 6.(d)), it is recommended to perform the perturbation tests with "0.5Hz" steps in low frequency ranges.

5) The couplings can be detected in the range of 0.01% pu-5% pu. This might lead to more precise measurement equipment (as used in the grid emulator) than the Class I requirement for frequency coupling detection purposes.

6) Considerable amplitudes of the MFCs are detected in the output current with a line as $\{f_h = 2f_0 - f_p\}$ in $I_{p(p)}$ for $\{f_h < 120\}$ (Fig. 6.(b)) and as $\{f_h = f_p - 2f_0\}$ in $I_{n(p)}$ for $\{f_h > 120\}$ (Fig. 6.(d)). This observation verifies the sequence exchange phenomenon depicted in (12).

7) According to Table I, the couplings in the positive sequence have "-$2f_0$" frequency shift with the couplings in the negative sequence. This finding proves that even the frequency couplings can cause corresponding MFC patterns with the "$2f_0$" frequency difference. This fact has been addressed in the proposed model in (15)-(18).

8) There is no considerable sequence coupling in the test results due to the symmetrical three-phase system. However, the proposed model can address any potential system asymmetry.

V. Conclusion

The frequency and sequence couplings can compromise the accuracy of multi-frequency models. In general, the frequency and sequence couplings can be created in a converter system due to the non-linear control, non-ideal DC-link, and asymmetry in a three-phase system. To the best of our knowledge, the couplings have been studied only as "$f_i \pm kf_0$, (k=1,2,...)" in the literature using linearized averaged models. While this paper reveals that the coupling patterns would be in more generic forms as "$\pm mf_i \pm kf_0$, (k=1,2,..., and m=1,2,...)" with multiples of the perturbation frequency and proposes a theory to explain the root-causes of it. In this way, more general forms of couplings are identified by extracting the empirical models through the Fourier transform of the switching converter response against perturbations. Furthermore, a methodology for determining the main couplings and generic multi-frequency modelling of converter-connected REGs is proposed. The proposed generic model is based on experimental small-signal perturbations. The proposed coupling patterns theory and the generic modelling methodology are verified using a 7MVA grid emulator for voltage perturbation tests on a 2MVA PV converter. Accordingly, a limited number of frequency couplings are observed in less than 1kHz, proving the practical application of the proposed methodology. Besides, the mirror frequency coupling concept (i.e., -$2f_0$ frequency shift) is observed among the couplings in positive and negative sequences and is called "Corresponding MFC" in this paper. The frequency couplings are mostly detected in the range of 0.01% pu- 5% pu in response to the small-signal perturbations (less than 2% pu). Thus, precise measurement equipment is required to identify the couplings. Besides, different noise levels in different frequency ranges are utilized as an adequate criterion for selecting the main coupling. Due to the similarities between converter-connected REGs, the methodology can be applied for modelling of Type 4 WTs as well.

The proposed methodology is focused on small-signal perturbations and modelling in the frequency domain and is not intended for large-signal variations and fault assessments. Besides, applying the proposed method for harmonic stability studies at the system level and evaluating the stochasticity effects of the renewable energy sources on the model parameters are left out for future works.

Acknowledgment

This work was authored in part by Alliance for Sustainable Energy, LLC, the manager and operator of the National Renewable Energy Laboratory for the U.S. Department of Energy (DOE) under Contract No. DE-AC36-08GO28308. Funding provided by the U.S. Department of Energy Office of Energy Efficiency and Renewable Energy Wind Power Technologies Office. The views expressed in the article do not necessarily represent the views of the DOE or the U.S. Government. The U.S. Government retains and the publisher, by accepting the article for publication, acknowledges that the U.S. Government retains a nonexclusive, paid-up, irrevocable, worldwide license to publish or reproduce the published form of this work or allow others to do so, for U.S. Government purposes.

References

[1] Ł.H. Kocewiak, J. Hjerrild and C.L. Bak, "Wind turbine converter control interaction with complex wind farm systems," in IET Renewable Power Generation, vol. 7, no. 4, pp. 380-389, July 2013.

[2] Buchhagen, C., Rauscher, C., Menze, A., and Jung, J.: BorWin1 – First Experiences with Harmonic Interactions in Converter Dominated Grids, Inter. ETG Cong., VDE VERLAG, 17–18 Nov., Berlin, Germany, 2015.

[3] H. Saad, Y. Fillion, S. Deschanvres, Y. Vernay, and S. Dennetière, "On resonances and harmonics in HVDC-MMC station connected to AC grid," IEEE Trans. Power Del., vol. 32, no. 3, pp. 1565–1573, Jun. 2017.

[4] Ł. H. Kocewiak, I. A. Aristi, B. Gustavsen and A. Hołdyk, "Modelling of wind power plant transmission system for harmonic propagation and small-signal stability studies," in IET Renewable Power Generation, vol. 13, no. 5, pp. 717-724, 8 4 2019, doi: 10.1049/iet-rpg.2018.5077.
[5] C. Li, "Unstable operation of photovoltaic inverter from field experiences," IEEE Trans. Power Del., vol. 33, no. 2, 1013–1015, Apr. 2018.
[6] J. Sun, G. Wang, X. Du and H. Wang, "A Theory for Harmonics Created by Resonance in Converter-Grid Systems," in IEEE Transactions on Power Electronics, vol. 34, no. 4, pp. 3025-3029, April 2019.
[7] IEC TR 61400-21-3: 2019 – Wind energy generation systems – Part 21-3: Measurement and assessment of electrical characteristics – Wind turbine harmonic model and its application, International Electrotechnical Commission, TC 88, ICS 28.180, 2019.
[8] X. Wang and F. Blaabjerg, "Harmonic Stability in Power Electronic-Based Power Systems: Concept, modelling, and Analysis," in IEEE Transactions on Smart Grid, vol. 10, no. 3, pp. 2858-2870, May 2019.
[9] X. Yue, X. Wang and F. Blaabjerg, "Review of Small-Signal modelling Methods Including Frequency-Coupling Dynamics of Power Converters," in IEEE Trans. on Pow. Electr., vol. 34, no. 4, pp. 3313-3328, April 2019.
[10] H. Yang, H. Just, M. Eggers and S. Dieckerhoff, "Linear Time-Periodic Theory Based modelling and Stability Analysis of Voltage Source Converters," in IEEE Journal of Emerging and Selected Topics in Power Electronics, doi: 10.1109/JESTPE.2020.3003379.
[11] S. Shah, P. Koralewicz, V. Gevorgian, H. Liu and J. Fu, "Impedance Methods for Analyzing Stability Impacts of Inverter-Based Resources: Stability Analysis Tools for Modern Power Systems," in IEEE Electrification Magazine, vol. 9, no. 1, pp. 53-65, March 2021.
[12] J. Sun, "Impedance-Based Stability Criterion for Grid-Connected Inverters," IEEE Tran. on Pow. Elec., vol. 26, no. 11, 3075-3078, Nov. 2011.
[13] M. Cespedes and J. Sun, "Impedance modelling and analysis of grid-connected voltage-source converters," IEEE Trans. Power Electron., vol. 29, no. 3, pp. 1254–1261, Mar. 2014.
[14] M. K. Bakhshizadeh et al., "Couplings in phase domain impedance modelling of grid-connected converters," IEEE Trans. Power Electron., vol. 31, no. 10, pp. 6792–6796, Oct. 2016.
[15] M. K. Bakhshizadeh, F. Blaabjerg, J. Hjerrild, Ł. Kocewiak and C. L. Bak, "Improving the Impedance-Based Stability Criterion by Using the Vector Fitting Method," in IEEE Transactions on Energy Conversion, vol. 33, no. 4, pp. 1739-1747, Dec. 2018, doi: 10.1109/TEC.2018.2849347.
[16] S. Shah and L. Parsa, "Impedance modelling of Three-Phase Voltage Source Converters in DQ, Sequence, and Phasor Domains" IEEE Trans. Energy Conversion, Vol. 32, NO. 3, 2017.
[17] T. Roinila, M. Vilkko, and J. Sun, "Online grid impedance measurement using discrete-interval binary sequence injection," IEEE Emerging and Selected Topics in Power Elect., vol. 2, no. 4, pp. 985–993, Dec 2014.
[18] Chauncey, G. L. (2018). Impedance Measurement Techniques in Noisy Medium Voltage Power Hardware-in-the-Loop Environments. Retrieved from http://purl.flvc.org/fsu/fd/2018_Su_Chauncey_fsu_0071N_14782
[19] A. Rygg, M. Molinas,C.Zhang, andX.Cai, "A modified sequence-domain impedance definition and its equivalent to the dq-domain impedance definition for the stability analysis of ac power electronic systems," IEEE J. Emerg. Sel. Topics Pow. Elect., vol. 4, no. 4, 1383–1396, Dec. 2016.
[20] V. Salis, A. Costabeber, S. M. Cox, F. Tardelli and P. Zanchetta, "Experimental Validation of Harmonic Impedance Measurement and LTP Nyquist Criterion for Stability Analysis in Power Converter Networks," in IEEE Trans. on Pow. Electr., vol. 34, no. 8, pp. 7972-7982, Aug. 2019.
[21] Nouri, B., Kocewiak, Ł., et al.: Test methodology for validation of multi-frequency models of renewable energy generators using small-signal perturbations. IET Renew. Power Gener. 1–13 (2021).https://doi.org/10.1049/rpg2.12245
[22] S. Azarian, P. Borowski, et al. "Experimental Impedance Measurement of SG DD-167 Variable-Speed Direct-Drive Wind Turbine by Power Electronic grid emulator of Fraunhofer IWES DyNaLab", 19th Wind Integration Workshop, Frankfort, 11-12 Nov., 2020.
[23] I. Vieto and J. Sun, "Sequence Impedance modelling and Converter-Grid Resonance Analysis Considering DC Bus Dynamics and Mirrored Harmonics," 2018 IEEE 19th Workshop on Control and modelling for Power Electronics (COMPEL), pp. 1-8, Padua, 2018.
[24] Y. Liao and X. Wang, "Stationary-Frame Complex-Valued Frequency-Domain modelling of Three-Phase Power Converters," IEEE Journal of Emerging and Selected Topics in Power Electronics, Vol. 8, No. 2, 2020.
[25] M. Cespedes and J. Sun, "Methods for stability analysis of unbalanced three-phase systems," 2012 IEEE Energy Convers. Congr. Expo. ECCE 2012, pp. 3090–3097, 2012, doi: 10.1109/ECCE.2012.6342511.
[26] H. Zong, C. Zhang, et al., "Block Diagonal Dominance-based Model Reduction Method Applied to MMC Asymmetric Stability Analysis," in IEEE Trans. on Ener. Conv., doi: 10.1109/TEC.2021.3054925.
[27] J. Sun and H. Liu, "Sequence Impedance modelling of Modular Multilevel Converters," in IEEE Journal of Emerging and Selected Topics in Power Electronics, vol. 5, no. 4, pp. 1427-1443, Dec. 2017.
[28] M. K. Bakhshizadeh, F. Blaabjerg, J. Hjerrild, X. Wang, Ł. Kocewiak and C. L. Bak, "A Numerical Matrix-Based Method for Stability and Power Quality Studies Based on Harmonic Transfer Functions," in IEEE Journal of Emerging and Selected Topics in Power Electronics, vol. 5, no. 4, pp. 1542-1552, Dec. 2017.
[29] H. Nian, L. Chen, Y. Xu, H. Huang and J. Ma, "Sequences Domain Impedance modelling of Three-Phase Grid-Connected Converter Using Harmonic Transfer Matrices," in IEEE Transactions on Energy Conversion, vol. 33, no. 2, pp. 627-638, June 2018.
[30] H. Zong, C. Zhang, J. Lyu, X. Cai, M. Molinas and F. Rao, "Generalized MIMO Sequence Impedance modelling and Stability Analysis of MMC-HVDC With Wind Farm Considering Frequency Couplings," in IEEE Access, vol. 8, pp. 55602-55618, 2020.
[31] H. Wang and J. Sun, "Impedance-Based Stability modelling and Analysis of Networked Converter Systems," 20th Workshop on Control and modelling for Power Elect. (COMPEL), pp. 1-8, Toronto, Canada, 2019.
[32] C. Zhang, M. Molinas, S. Føyen, J. A. Suul and T. Isobe, "Harmonic-Domain SISO Equivalent Impedance modelling and Stability Analysis of a Single-Phase Grid-Connected VSC," in IEEE Transactions on Power Electronics, vol. 35, no. 9, pp. 9770-9783, Sept. 2020.
[33] S. S. Thakur, M. Odavic, and et. al. "Theoretical Harmonic Spectra of PWM Waveforms Including DC Bus Voltage Ripple—Application to a Low-Capacitance Modular Multilevel Converter," in IEEE Transactions on Power Electronics, vol. 35, no. 9, pp. 9291-9305, Sept. 2020.
[34] Y. Jian and A. Ekstrom, "General analysis of harmonic transfer through converters," IEEE Trans. Pow. Elec., vol. 12, no. 2, pp. 287–293, 1997.
[35] S. Alepuz et al., "Control Strategies Based on Symmetrical Components for Grid-Connected Converters Under Voltage Dips," in IEEE Transactions on Industrial Electronics, vol. 56, no. 6, pp. 2162-2173, 2009.
[36] ŁH Kocewiak, BLØ Kramer, et al. "Resonance damping in array cable systems by wind turbine active filtering in large offshore wind power plants" IET Ren. Pow. Gen. 11 (8), 1069-1077.
[37] Electromagnetic compatibility (EMC) – Part 3-6: Limits – Assessment of emission limits for the connection of distorting installations to MV, HV and EHV power systems. International Electro-technical Commission, TC 77, TC 77/SC 77A, eddition 2, 2008.
[38] Electromagnetic compatibility (EMC) – Part 4-7: Testing and measurement techniques – General guide on harmonics and interharmonics measurements and instrumentation, for power supply systems and equipment connected thereto. International Electro-technical Commission, TC 77/SC 77A, 2.1 Edition, Oct. 2009.
[39] Ł. H. Kocewiak, J. Hjerrild and C. L. Bak, "The impact of harmonics calculation methods on power quality assessment in wind farms," Proceedings of 14th International Conference on Harmonics and Quality of Power - ICHQP 2010, pp. 1-9, Bergamo, 2010.
[40] B. Nouri, Ö. Göksu, V. Gevorgian, and Poul E. Sørensen "Generic characterization of electrical test benches for AC- and HVDC-connected wind power plants" Wind Energ. Sci., 5, 561–575, 2020, https://doi.org/10.5194/wes-5-561-2020.
[41] B. Nouri, Ł. Kocewiak, and P. Sørensen, "Frequency and Sequence Couplings in Type 4 and Type 3 Wind Turbines" 19th Wind Integration Workshop, 11-12 November 2020, Frankfort, Germany, 2020.

Behnam Nouri (S'18) received the B.Sc. degree in Electrical Engineering from the University of Tabriz, Tabriz, Iran, in 2012. In 2015, he received the M.Sc. degree in Power Electronics and Electrical Machines from the University of Tehran, Tehran, Iran. He joined the Department of DTU Wind Energy at the Technical University of Denmark in 2018, where he has pursued a PhD.

From 2015 to 2018, he was an R&D Engineer with Technic Control Co., Tehran, Iran. He is an official member of IEC Technical Committee 88 and Danish Standard 588 contributing to electrical assessment of wind energy since 2020. His research interests include power electronics and its applications, power quality and harmonics, control and modelling of converter-based systems, and model validation and grid code compliance tests.

Łukasz Kocewiak (M'12–SM'16) received the B.Sc. and M.Sc. degrees in electrical engineering from the Warsaw University of Technology, Warszawa, Poland, in 2007, and the Ph.D. degree from Aalborg University, Aalborg, Denmark, in 2012. He is currently a Research and Development Manager and a Senior Power System Engineer on the development of electrical infrastructure in large offshore wind power plants with Ørsted Wind Power, Fredericia, Denmark. He has authored or co-authored more than 70 publications.

His current research interests include harmonics and nonlinear dynamics in power electronics and power systems, especially on wind power generation units. Łukasz is a member of various working groups or activities within CIGRÉ and IEC.

Shahil Shah (M'18-SM'21) received the B.E. degree from Government Engineering College, Gandhinagar, India, in 2006, the M.Tech. degree from the Indian Institute of Technology (IIT) Kanpur, Kanpur, India, in 2008, and the Ph.D. degree from Rensselaer Polytechnic Institute (RPI), Troy, NY, in 2018, all in Electrical Engineering. He is currently a senior engineer in the Power Systems Engineering Center of the National Renewable Energy Laboratory (NREL), Golden, CO. His research focusses on dynamic and transient stability of renewable energy systems and power systems with high levels of inverter-based resources. He is serving as an editor of the IEEE Transactions on Energy Conversion.

Shahil was the recipient of the 2018 RPI Allen B. Dumont prize, given to a doctoral "who demonstrates candidate high scholastic ability and makes substantial contribution to his/her field."

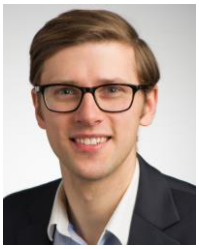

Przemyslaw Koralewicz (M'17) received his MSEE from Silesian Technical University in Gliwice, Poland in 2010. He specializes in modelling, detailed analysis and testing of smart inverters and complex power systems including microgrids.

He is utilizing the NREL Controllable Grid Interface (CGI), a new, groundbreaking testing apparatus and methodology to test and demonstrate many existing and future advanced controls for various renewable generation technologies on the multimegawatt scale and medium-voltage levels.

Vahan Gevorgian (M'97–SM'17) received the Ph.D. degree in electrical engineering from the State Engineering University of Armenia, Yerevan, Armenia, in 1993. He joined NREL in October 1994 and has served many roles over the years. He is currently working with the Power Systems Engineering Center focused on renewable energy impacts on transmission and interconnection issues and dynamic modelling of variable generation systems. He is involved in many different areas, including dynamometer and field testing of large and small wind turbines, dynamometer testing of wind turbine drive-train, development of advanced data acquisition systems, and wind turbine power quality.

Vahan provides technical support to NREL industry partners and major US wind turbine manufacturers. He is a member of the IEC team for wind turbine power quality. His contributions to NREL research have been recognized through multiple Outstanding Individual and Team Staff Awards.

Poul Sørensen (SM'07, F'21) is Professor in wind power integration and control in the Department of Wind Energy at the Technical University of Denmark. He was born in 1958 and received M.Sc. degree in electrical engineering from DTU in 1987. He is Convener of IEC 61400-27 electrical simulation models for wind power generation. He is also Principal Investigator and Work Package leader in several research projects and has supervised 20 PhD students and 30 Master's thesis.

He has been editor of Wiley Wind Energy 2007-13. He has been IEEE Senior Member since 2007, and he became IEEE Fellow Member in 2021 for his "contributions to wind power converter control and grid integration."